# Dissolution Kinetics, Step and Surface Morphology of Magnesite (104) Surfaces in Acidic Aqueous Solution at 60 °C by Atomic Force Microscopy under Defined Hydrodynamic Conditions

**Steven R. Higgins,\*,†,∥ Lawrence H. Boram,† Carrick M. Eggleston,† Barry A. Coles,‡ Richard G. Compton,‡ and Kevin G. Knauss§**

*Department of Geology and Geophysics, University of Wyoming, Laramie, Wyoming 82071, Physical and Theoretical Chemistry Laboratory, Oxford University, South Parks Road, Oxford OX1 3QZ, United Kingdom, and Geoscience and Environmental Technology Division, Lawrence Livermore National Laboratory, L-202, Livermore, California 94550*

Dissolution of the (104) surface of magnesite ($MgCO_3$) was studied as a function of bulk solution pH over the range $2.0 < pH < 5.0$ at 60 °C using atomic force microscopy (AFM) with well-defined hydrodynamics. The experimental data and corresponding solution of the convective-diffusion equation for the system revealed that magnesite dissolution is kinetically inhibited by a factor of $10^2$–$10^4$ relative to the proton mass transport limit. The dissolution flux was found to vary nonlinearly with the surface concentration of $H^+$, $[H^+]_{y=0}$, and that inclusion of the homogeneous chemical kinetics of $H^+$ consumption in the system to form carbonic acid was unnecessary. The nonlinear behavior was best represented by a Langmuir isotherm for proton adsorption in which the adsorbed entity consists of a surface complex containing more than one proton. The apparent surface kinetic detachment coefficient, $k'_n$, for this surface complex was determined to be $5 \times 10^{-12}$ mol cm$^{-2}$ s$^{-1}$, but the determination of a particular coordination number, $n$, of this detachment complex was not possible based on the experimental data. The velocity of dissolving + steps was found to be constant, within error, over the entire experimental pH range, whereas the dissolution flux varied by over an order of magnitude in this same range. The AFM images revealed a dramatic increase in step density associated with a large increase in dissolution flux that was attributed to the protonation of terrace-adsorbed carbonate sites (i.e., adions). We propose that the intrinsic protonation constant, $K_{int}$, differs for adions, kink, step, and terrace sites based on the AFM observations of surface and step morphology as a function of pH.

## 1. Introduction

The dissolution and precipitation of carbonate minerals such as calcite, magnesite, and dolomite are chemical processes with a globally important role in controlling aspects of soil, groundwater, and atmospheric chemistry. For an environmentally important example, soil specimens in the Vadose Zone at the Hanford, Washington (USA) radioactive waste storage facility have been found to contain calcium carbonate as a ubiquitous mineralogical component.[1] The exchange of waste cations, such as $Sr^{2+}$ and $Co^{2+}$ that have leaked from failing storage tanks, with $Ca^{2+}$ in the calcite grain coatings may inhibit the migration of these cations toward the water table. On a global scale, the formation of carbonate minerals (especially calcite) following chemical weathering of calcium silicate minerals plays a vital role in reducing levels of atmospheric $CO_2$ over long periods of time.[2,3] Recently, it was suggested that this process could be brought to the human time scale so that carbonate mineral precipitation could be exploited in a solid-phase $CO_2$ sequestration strategy.[4,5] The strategy involves the dissolution of alkaline earth silicate minerals in aquifers coupled with the precipitation of alkaline earth and other carbonates during and following the injection of $CO_2$ into the subsurface environment.

To deal with these very complicated problems requires knowledge of numerous coupled chemical and physical processes. Amidst this complex physicochemical problem lie fundamental heterogeneous chemical reactions that contribute to the homogeneous chemical composition of the liquid phase. It is our goal here to examine the heterogeneous kinetics of a relatively simple solid/liquid interface (e.g., magnesite/water) in an experimental configuration that allows full consideration of the chemical kinetics and hydrodynamics.

Aqueous dissolution of calcite in acidic solution has been the subject of a substantial literature.[6–13] In general, dissolution of materials such as calcite is under mixed kinetics/transport control. Limiting behavior is governed by extremely sluggish heterogeneous chemical reactions in a purely kinetically controlled reaction and by mass transport in the case of infinitely fast heterogeneous kinetics. Because few systems can be generically classified as belonging to either of these two limiting cases, mass transport must be well-defined and controllable in order to quantitatively treat any system falling into the continuum of mixed reaction control. One pitfall for experimental methods utilizing closed or mixed-flow stirred tank reactors containing solid particulate suspensions is that dissolution fluxes may depend on particle size, shape, weight percent of solid, and reactor geometry as it relates to the action of the stirring

------

\* To whom correspondence should be addressed. Fax: 1−307-766-6679. E-mail: shiggins@uwyo.edu.
† Department of Geology and Geophysics, University of Wyoming.
‡ Physical and Theoretical Chemistry Laboratory, Oxford University.
§ Geoscience and Environmental Technology Division, Lawrence Livermore National Laboratory.
∥ Present address: Chemistry Department, Wright State University, Dayton, OH 45435.

mechanism. In stirred suspensions, mass transport in the system is neither controlled, nor is it well defined.

A quantitative measurement of heterogeneous reaction kinetics and its relative importance in the overall impedance to the reaction flux is generally not possible without knowledge of relevant fluid velocities. This point was discussed in Compton and Unwin[10] and led them to examine the attributes of a more rigorous experimental approach in examining the kinetics of calcite dissolution. Among these attributes are well-defined and controllable fluid inlet chemistry and the controlled and calculable delivery of the inlet solution to the solid sample surface. The channel flow cell (CFC) experimental method (see, for example, Unwin et al.[14]) contains these attributes. In the CFC methodology, a sample is embedded and polished into the wall of one side of a rectangular duct whose fluid flow dynamics are known. The laminar flow characteristics of the CFC permit calculation (either analytical or numerical) of the response of a detector situated downstream of the sample for a given sample surface rate function (i.e., heterogeneous "rate law") and as a function of flow rate. Thus, fluid flow rate is utilized as an independent variable in the experimental methodology.

A limitation to the CFC approach is that the kinetic information obtained represents essentially an average over the entire solid surface. Little in the way of microscopic detail may be obtained from this experiment and thus, attempting to understand how the macroscopic observations relate to the microscopic surface processes (e.g., step motion, step bunching, and pit nucleation) may only be inferred after ex-situ examination of the surface morphology. The possible application of advanced interferometric optical microscopy[15,16] may prove to be valuable in this type of experimental configuration.

Currently, microscopic in-situ observations of solid surfaces undergoing chemical or electrochemical reactions are facilitated with fluid cells designed for scanning probe microscopes. Such studies allow us to visualize and quantify microscopic processes that we may otherwise only infer from theoretical models or lower resolution, ex-situ imaging methods. Unfortunately, fluid velocities in most AFM fluid cells are unknown and difficult to predict. In ill-defined flow systems associated with many AFM experiments, it is a widely accepted practice to stipulate that surface kinetics limited conditions exist when observed flux is independent of fluid flow. In fact, this type of conclusion is largely based on essentially qualitative data. There is no method (when hydrodynamics are unknown) of quantitatively predicting how flux will vary with total flow. There is, furthermore, no guarantee that the magnitudes of the relevant fluid velocity vectors will scale linearly with total flow or that the flow patterns in the fluid cell will not undergo wholesale changes as flow rate is varied. It is therefore only possible to stipulate the chemical conditions at the surface of the sample undergoing reaction, and the validity of such stipulations cannot be tested without knowing the fluid transport conditions. It is then possible to suggest that experiments performed in systems where hydrodynamics are unknown, may not be comparable at a quantitative level, and it is reasonable to infer that without controllable and predictable mass transport, it is a rather daunting task to reconcile experimental discrepancies. There are, of course, other factors that may give rise to differing experimental results, but the purpose here was to deal with but one of these factors.

To observe microscopic phenomena with AFM while maintaining the experimental attributes mentioned above, Coles et al.[11,17] designed a precision inlet duct for a commercial AFM system, modeled the fluid dynamics (as a function of Reynolds number, Re) over a sufficiently large volume of fluid encompassing the AFM cantilever and sample surface, and validated the hydrodynamic modeling in a well-characterized electrochemical system. Unfortunately, the dynamic range of AFM as a tool for measuring net flux is rather limited (the low end depending on the perseverance of the experimentalist, and the high end by the limited vertical range of the piezoelectric scanner). There exists a narrow window of fluxes that are suitable for measurement with AFM. The microscopic study of heterogeneous kinetics for a material kinetically less facile than calcite, for example, often requires elevated temperatures.[16,18−20] By elevating the temperature of the system, mass transport usually becomes a more important consideration and it is wise to therefore quantitatively account for mass transport rather than to rely on difficult-to-test assumptions. For this paper, we have adapted the Coles et al.[11,17] inlet duct to a previous design for the hydrothermal AFM (HAFM)[21] and utilize this experimental apparatus in the study of heterogeneous kinetics of magnesite (104) dissolution in acidic aqueous solutions.

## 2. Experimental Section

**2.1 Materials.** The magnesite crystals originated in Brumado, Brazil. Electron microprobe analysis showed less than 0.1 mol % Ca and traces of Fe with possibly trace amounts of Mn, Cu, and Zn ($\leq$0.01 mol %).[20] The aqueous solutions were prepared by adding reagent grade $HNO_3$ to 0.1 M $NaNO_3$ in deionized water (resistivity: 18 M$\Omega$ cm). The solutions were adjusted to the desired pH (2.0−5.0) at room temperature. Aqueous speciation calculations demonstrated that the pH of these solutions would change immeasurably upon heating to 60 °C, the temperature employed in all experiments. All experiments were performed under 10.0 $\pm$ 0.5 bar $N_2$, which is not expected to change any relevant chemical equilibrium constants.

$Mg^{2+}$ activities, $a(Mg^{2+})$, of the inflowing solutions were based on maximum Mg concentrations in the reagents (50 ppm in reagent grade $NaNO_3$). The activity of $CO_3^{2-}$, $a(CO_3^{2-})$, was calculated at each pH condition by assuming equilibrium of the fluid with respect to the atmosphere (i.e., $CO_2$ (g)) during solution preparation and prior to sealing and pressurizing the fluid with $N_2$, The initial $a(Mg^{2+})$ therefore was $10^{-5.7}$ and $a(CO_3^{2-})$ was $10^{-17.67}$, $10^{-15.27}$, $10^{-13.27}$, and $10^{-11.65}$ at pH = 2, 3.2, 4.2, and 5.0, respectively. $K_{sp}$ for $MgCO_3$ at 60 °C is $10^{-8.69}$. All activities and equilibrium constants above were based on calculations using the EQ3/6 thermodynamic code and database.

**2.2 Methods.** *2.2.1 AFM Apparatus and Fluid Cell Hydrodynamics.* For the experiments, we used a continuous-flow, single-pass, hydrothermal atomic force microscope described by Higgins et al.[21] and modified to conform to the inlet configuration and dimensions utilized in a recent ambient AFM fluid cell modification.[11] Fluid was contained in a pressurized Viton bladder accumulator or passivated Ti bomb (at room temperature), both serving as feed sources for the AFM fluid cell. A 90 W temperature controlled aluminum heater plate containing a length of Ti tubing (0.5 mL internal volume) was used just upstream of the AFM fluid cell to preheat the fluid to the desired cell temperature. A ring heater under separate temperature control surrounded the fluid cell and was used to maintain the temperature of the fluid cell body. Precise temperature control is not possible without immersing the entire microscope in a heated enclosure, so the actual temperature of the fluid is likely to differ from the reported temperature of 60 °C by up to 1−2 °C. Flow rates were controlled (accurate to $\pm$ 1%) downstream of the fluid cell by a fluid mass flow controller.

The hydrodynamics within a volume of fluid extending from the mouth of the inlet to beyond the position of the AFM cantilever were modeled at various Re and the resulting three-dimensional fluid velocity data are available on the World Wide Web.[22] These fluid velocities were calculated assuming water properties at 25 °C. Any particular velocity file generated at 25 °C with a characteristic Re will represent identical flow patterns for any other temperature, at a different volume flow rate. By determining the volume flow rate required to obtain the same Re at the desired temperature as is given for the Re at 25 °C, then for a given velocity map, the fluid velocities are simply multiplied by a scaling factor, $V_{sc}$, according to

$$V_{sc} = \frac{V_f(T)}{V_f(25\ °C)} = \frac{\eta(T)\rho(25\ °C)}{\eta(25\ °C)\rho(T)} \tag{1}$$

where $\eta(T)$ and $\rho(T)$ are the absolute water viscosity and density, respectively at temperature $T$.

*2.2.2 AFM Imaging and Dissolution Flux Measurements.* The HAFM was operated in contact mode using uncoated silicon cantilevers (Nanosensors) with a nominal force constant of 0.2 N/m. The contact force was usually maintained below 10 nN, but to address the possible influence of the AFM tip on the experimental observations, occasional examination of the surface surrounding the repetitively imaged area was performed. No evidence was found for substantial enhancement or inhibition of the local dissolution flux that could be attributed to the presence and/or action of the AFM tip/cantilever.

The net dissolution flux from the magnesite surface was determined by the method of counting the number of elementary layers, of height $h$ ($h = 2.7$ Å on magnesite(104)), that had dissolved (over a known period of time) at a fixed location (i.e., the imaged area) on the surface to yield the layer dissolution frequency, $\omega$. The net dissolution flux is then related to the number of layers dissolved per unit time, $\omega$, by

$$J(\text{mol·cm}^{-2}\text{s}^{-1}) = \frac{\omega \cdot h}{\Omega} \tag{2}$$

where $\Omega$ is the molar volume of the crystal. An equivalent approach involves the measurement of step velocity, $v_{step}$ (perpendicular to the mean step orientation utilizing a surface landmark as a fixed point of reference), and step density, $\rho_{step}$, for corresponding steps to give $\omega$

$$\omega = \rho_{step} v_{step} \tag{3}$$

Due to the very small net dissolution frequency of magnesite (relative to microscope drift) under the range of experimental conditions, we were unable to utilize the change (with time) in the feedback voltage applied to the vertical piezoelectric scanner electrode to determine the dissolution flux.[23,24]

*2.2.3 Mass Transport in the AFM.* The solution to the steady-state convective-diffusion equation in the absence of homogeneous chemical reactions (eq 4), subject to appropriate boundary conditions, provides the concentration of, for example, a reactant, $R$, everywhere in a system for which fluid velocities, $v(x, y, z)$, are defined

$$\frac{\partial[R]}{\partial t} = 0 = D_R \nabla^2[R] - v_x\frac{\partial[R]}{\partial x} - v_y\frac{\partial[R]}{\partial y} - v_z\frac{\partial[R]}{\partial z} \tag{4}$$

In the above equation, it is implied that $[R]$, $v_x$, $v_y$, $v_z$, the concentration and fluid velocities, are all functions of position $(x, y, z)$ and $D_R$ is the diffusion coefficient of $R$. As described previously,[25] we may simplify eq 4 in the problem associated
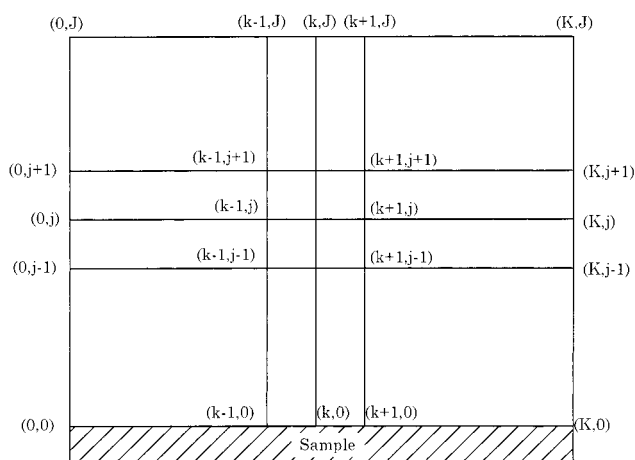


**Figure 1.** Two-dimensional BIFD grid used in the numerical solution to eq 7. The grid size used in all calculations was K = J = 500 points.

with the experimental geometry by mapping $v_x$ and $v_z$ onto a new coordinate, $d$, which is curved in $x,z$ space (and parallel to the sample surface) and traces the particle path leading from the mouth of the duct to the AFM tip position. By assuming that diffusion along $x$ and $z$ is negligible, then eq 4 can be further simplified to

$$0 = D_R\frac{\partial^2[R]}{\partial y^2} - v_y\frac{\partial[R]}{\partial y} - v_d\frac{\partial[R]}{\partial d} \tag{5}$$

Should there be any homogeneous consumption of $R$ in the system, this will require an additional term (in $R$) for eqs 4 and 5. This homogeneous chemical term in the acidic dissolution of magnesite is due to the protonation of bicarbonate to form carbonic acid and the subsequent dehydration of carbonic acid to form aqueous $CO_2$

$$H^+ + HCO_3^- \leftrightarrow H_2CO_{3(aq)} \tag{a}$$

$$H_2CO_{3(aq)} \rightarrow CO_{2(aq)} + H_2O \tag{b}$$
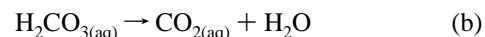
In the proton-promoted dissolution of magnesite with consideration of these homogeneous chemical kinetics, it is necessary to write two convective diffusion equations, one in reactant $H^+$, and another in the product $HCO_3^-$.

**Numerical Solution.** Equation 5, as it applies to the current problem, cannot be solved analytically because $v_y(x, d)$ and $v_d(x, d)$ are complicated, and we therefore utilize a method of finite differences to numerically solve the equation. Specifically, we employ the Backward Implicit Finite Difference (BIFD) method to the problem (see Morton[26] for a mathematical description of the method and refs 27 and 28 for other applications of the BIFD method to the CFC). The solution is facilitated by generating a two-dimensional finite difference grid (see Figure 1) consisting of velocity vectors $v_d$ and $v_y$ at evenly spaced intervals $\Delta d$ and $\Delta y$ which are defined by

$$d_k = k\Delta d \quad k = 0, 1, ..., K \text{ and } \Delta d = (d_e - d_s)/K$$

$$y_j = j\Delta y \quad j = 0, 1, ..., J \text{ and } \Delta y = h/J$$

where the number of grid points in the $d$ and $y$ directions is $K + 1$ and $J + 1$, respectively, $d_e$ and $d_s$ are the respective ending and starting positions of the grid along $d$, and $h$ is the maximum height of the grid above the surface ($y$ dimension). To obtain an accurate solution, $h$ must be greater than the diffusion layer

thickness. Setting $C = [R]$ for simplicity, eq 5 may be written approximately as

$$0 = D\frac{C_{j+1,k+1} - 2C_{j,k+1} + C_{j-1,k+1}}{(\Delta y)^2} - v_y \frac{C_{j,k+1} - C_{j-1,k+1}}{\Delta y} -$$
$$v_d \frac{C_{j,k+1} - C_{j,k}}{\Delta d} \quad (6)$$

Solving for $C_{j,k}$ generates the general set of finite difference equations for this problem, neglecting any homogeneous chemical reactions

$$C_{j,k} = aC_{j-1,k+1} + bC_{j,k+1} + cC_{j+1,k+1} \quad (7)$$

where the coefficients $a$, $b$, and $c$ are defined as

$$a = -(\lambda_y + \lambda_{v_y})/\lambda_{v_d}, \, b = (2\lambda_y + \lambda_{v_y} + \lambda_{v_d})/\lambda_{v_d}$$
$$c = -\lambda_y/\lambda_{v_d}$$

and

$$\lambda_y = \frac{D}{(\Delta y)^2}, \, \lambda_{v_y} = \frac{v_y}{\Delta y}, \, \lambda_{v_d} = \frac{v_d}{\Delta d}$$

and $v_y$ and $v_d$ are implicit functions of position $(d, y)$ in the finite difference grid. Equation 7 above represents a $(J - 1) \times (J - 1)$ matrix equation. To solve this set of equations, we must first specify the relevant boundary conditions which are defined when $k = 0$ (upstream edge of the crystal), $j = 0$ (surface of the crystal), and $j = J$ (far edge of the fluid volume, opposite the crystal surface, for which fluid velocities are defined). When $k = 0$ (i.e., the starting position along the $d$-coordinate)

$$C_{j,0} = C_{\text{inlet}} \quad (8)$$

where $C_{\text{inlet}}$ is the inlet concentration of the reactant, in this case, $H^+$. When $j = J$, the furthest edge from the surface in the BIFD grid

$$\left(\frac{\partial C}{\partial y}\right)_{J,k} = 0 \Rightarrow C_{J-1,k} = C_{J,k} \quad (9)$$

This is a no-flux boundary condition implying that the flux of reactants toward the surface is confined to a diffusion layer thickness that is smaller than $h$. Finally, when $j = 0$ (i.e., the surface of the solid) we must choose a candidate heterogeneous rate function $f(C_{0,k})$ where the net flux of reactant $J_C$ is

$$J_C = -D\left(\frac{\partial C}{\partial y}\right)_{j=0} = f(C_{0,k}) \quad (10)$$

We will first consider the case in which the heterogeneous consumption of $H^+$ is transport limited (see Suarez et al.[29] for application of this condition to dissolution of MgO), implying that the surface concentration of $H^+$, $C_{0,k}$, is very small compared to the bulk concentration, and for all practical purposes, the boundary condition eq 10 is

$$C_{0,k} = 0 \quad (10\text{-}1)$$

The first equation (i.e., $j=1$) in eq 7 may be written

$$C_{1,k} = aC_{0,k+1} + bC_{1,k+1} + cC_{2,k+1} \quad (11)$$

where the first term on the right-hand side is zero from the boundary condition eq (10−1). By incrementing $j$, the entire matrix, eq 7, is generated

$$\{d\}_k = [T]\{u\}_{k+1}$$

$$\begin{vmatrix} d_1 \\ d_2 \\ \vdots \\ d_j \\ \vdots \\ d_{J-2} \\ d_{J-1} \end{vmatrix} = \begin{vmatrix} b_1 & c_1 & & & & \\ a_2 & b_2 & c_2 & & & \\ & \vdots & \vdots & \vdots & & \\ & & a_j & b_j & c_j & \\ & & & \vdots & \vdots & \vdots \\ & & & & a_{J-2} & b_{J-2} & c_{J-2} \\ & & & & & a_{J-1} & b_{J-1} \end{vmatrix} \begin{vmatrix} u_1 \\ u_2 \\ \vdots \\ u_j \\ \vdots \\ u_{J-2} \\ u_{J-1} \end{vmatrix}$$

where the vectors, $d_j$, are

$$d_1 = C_{1,k} = b_1 C_{1,k+1} + c_1 C_{2,k+1}$$
$$d_j = C_{j,k} = a_j C_{j-1,k+1} + b_j C_{j,k+1} + c_j C_{j+1,k+1}$$

and employing the no-flux boundary condition eq 9

$$d_{J-1} = C_{J-1,k} = a_{J-1}C_{J-2,k+1} + (b_{J-1} + c_{J-1})C_{J-1,k+1}$$

By employing the boundary condition eq 8, all vectors in $\{d\}_{k=0}$ are set equal to $C_{\text{inlet}}$. From $\{d\}_0$, $\{u\}_1$ is evaluated by solving the tridiagonal matrix equation using the Thomas algorithm.[30,31] Because $\{d\}_k = \{u\}_k$ in the case where homogeneous chemical reactions are ignored, $\{d\}_1$ is obtained from $\{u\}_1$, thus allowing $\{u\}_2$ to be evaluated, and so forth until $\{u\}_K$ is found. In this manner, all values $C_{j,k}$ are determined and the flux at any surface position, $(k, j = 0)$, along the finite difference grid may be calculated, subject to the transport-limited boundary condition

$$J_C(k) = -D\left(\frac{C_{1,k} - C_{0,k}}{\Delta y}\right) = -D\left(\frac{C_{1,k}}{\Delta y}\right) \quad (12)$$

## 3. Results

The experimental data for the dissolution flux of magnesite obtained as a function of flow rate is shown in Figure 2 for various values of pH$_{\text{inlet}}$. The data clearly show that pH has a definite influence on the dissolution flux, and that there is no significant increase in dissolution flux with increase in flow rate. To apply the proton diffusion-limited test case to the experimental data, we assume that the magnitude of the proton flux toward the surface equals the magnitude of the magnesite dissolution flux.

Figure 2a shows the BIFD prediction for the diffusion-limited test case in comparison to the experimental data. When eq 7 is evaluated from the BIFD calculations for each of the experimental values of $C_{\text{inlet}}$, and using $D_{H+} = 1.49 \times 10^{-4} \text{ cm}^2 \text{ s}^{-1}$ at 60 °C from extrapolation of the 5−55 °C data from Harned and Owen,[32] the magnitude of the calculated proton flux is at least two orders (and in some cases four orders) of magnitude higher than the observed dissolution flux. From a check of the true equilibrium constant for $H_2CO_3$ deprotonation, $K_a =1.7 \times 10^{-4}$ M at 25 °C (see Compton and Unwin[10]), it is clear that at the pH values employed in the experiments, initial neglect of the homogeneous chemical reactions a and b is unjustified. For our experiments at 60 °C, we will use a value of $K_a = 1.5 \times 10^{-4}$ M based on extrapolation of the 5−45 °C data of Wissbrun et al.,[33] and a value of $k_b = 330 \text{ s}^{-1}$ based on extrapolation of
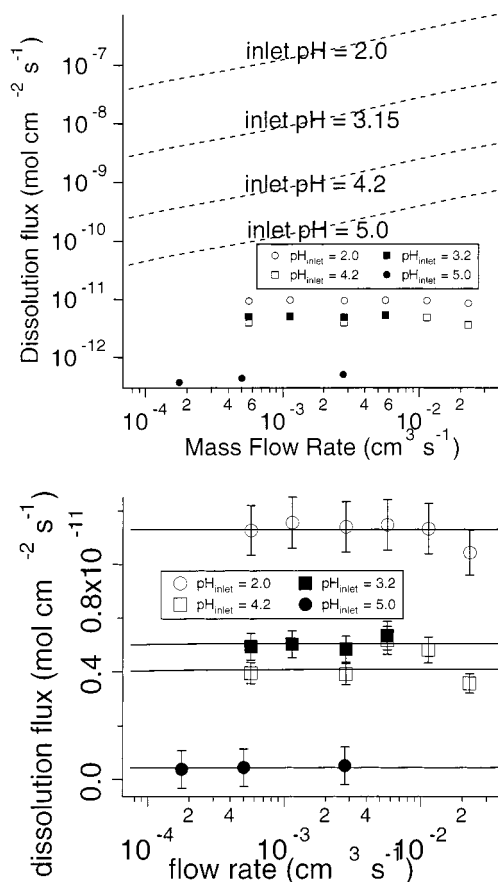
**Figure 2.** Observed dissolution flux as a function of volume flow rate at 60 °C at various inlet pH conditions. The flux was measured locally by analysis of sequences of AFM images. (a) Comparison of the experimental data from Figure 1 with the predicted flux based on solution of the convective-diffusion equation for the case of transport-limited flux of protons toward the surface. (b) Predicted flux in comparison to observed flux assuming a 1st order heterogeneous mechanism. The 1st order heterogeneous rate constant, $k_1$, was not independent of pH, but varied from $1 \times 10^{-6}$ cm s$^{-1}$ (pH = 2.0) to 4.5 $\times 10^{-5}$ cm s$^{-1}$ (pH = 5.0).

the 3.5−38.5 °C data (in 0.5 M NaCl) of Patel et al.[34] At most, the inclusion of the homogeneous reactions would reduce the calculated flux by a factor of 1/2 because for every proton consumed by the formation of bicarbonate, a second proton would be consumed in the formation of carbonic acid in homogeneous solution. This would not account for the discrepancy between diffusion limited flux and observed flux, and thus the conclusion is that acidic dissolution of magnesite under all but nearly stagnant flow conditions is controlled by the kinetics of heterogeneous reactions.

By modifying the boundary condition eq 10 to include a heterogeneous rate function, we create an adjustable parameter (i.e., the heterogeneous rate constant) that provides a degree of freedom by which to fit the experimental data. Because the data show virtually no variation in dissolution flux with flow rate, any arbitrary heterogeneous rate function will suffice to generate a fit. We can make the following 1st order mechanistic assumption based on the calcite study by Compton and Unwin[10]

$$J_{MgCO_3} = -D_{Mg^{2+}}\left(\frac{\partial[Mg^{2+}]}{\partial y}\right)_{y=0} = D_{H^+}\left(\frac{\partial[H^+]}{\partial y}\right)_{y=0} =$$

$$k_1[H^+]_{y=0} \quad (13)$$

Equation 13 was generalized to arbitrary reaction order, $n$, with respect to proton concentration by Compton and Unwin, but we will show that in our analysis of the experimental data, examination of the $n = 1$ case is sufficient. Equation 10 for this case can be approximated by

$$D_C\left(\frac{C_{1,k} - C_{0,k}}{\Delta y}\right) = k_1 C_{0,k}$$

Upon rearranging $C_{0,k}$ is obtained

$$C_{0,k} = \left(\frac{D_C}{D_C + k_1\Delta y}\right)C_{1,k} \quad (14)$$

Substituting this expression into eq 7 ($j = 1$), we obtain a modified value for $b_1$

$$b_1 = \frac{-(\lambda_y + \lambda_{v_y})D_C}{\lambda_{v_d}(D_C + k_1\Delta y)} + \frac{2\lambda_y + \lambda_{v_y} + \lambda_{v_d}}{\lambda_{v_d}}$$

The value of $b_1$ in the general case of an $n^{th}$ order heterogeneous mechanism was given in Compton and Unwin.[10] All other vector and matrix elements are the same as in the diffusion-limited case. The results of the BIFD calculations are shown as fits to the experimental data in Figure 2b for various values of pH$_{inlet}$. Although the lack of influence of flow rate on observed flux makes the choice of boundary condition eq 10 arbitrary, the values obtained for $k_1$ are not independent of $C_{inlet}$, suggesting that the heterogeneous rate function in eq 13 is not applicable over the entire pH range 2.0 < pH < 5.0. We still need to consider the influence of homogeneous chemical reactions a and b on the rate constants.

We recall that in the absence of homogeneous chemical reactions, $\{d\}_k = \{u\}_k$ and evaluating $C_{j,k}$ everywhere simply proceeds downstream starting from $k = 0$. By including the homogeneous reactions a and b, we must write two mass transport equations to account for the transport of H$^+$ and HCO$_3^-$ as well as the homogeneous chemical consumption of these species. Compton and Unwin[10] found that the homogeneous term, accounting for the protonation/deprotonation of bicarbonate/carbonic acid and subsequent decomposition of carbonic acid (reactions (a) and (b)), was (see Appendix A for derivation)

$$\frac{d[H^+]}{dt} = \frac{d[HCO_3^-]}{dt} = \frac{-k_{H_2CO_3}[H^+][HCO_3^-]}{K_{H_2CO_3} + [H^+] + [HCO_3^-]} \quad (15)$$

For convenience, we will now make the following definitions

$$C_{j,k}^{H^+} = [H^+]_{j,k}, \quad C_{j,k}^{HCO_3^-} = [HCO_3^-]_{j,k}$$

The modification of the Finite Difference convective diffusion eq 7 for both H$^+$ and HCO$_3^-$, by eq 15 was given in Compton and Unwin.[10] We estimated $D_{HCO3-}$, the bicarbonate diffusion coefficient at 60 °C to be $2.0 \times 10^{-5}$ cm$^2$ s$^{-1}$ by assuming the temperature dependence of $D_{HCO3-}$ is similar to that of $D_{H+}$.

The consideration of the homogeneous chemical reactions has a negligible influence on the near surface chemistry within the diffusion layer as evidenced by the calculated values for $C_{0,k}^{H^+}/C_{j,0}^{H^+}$ vs $k$ (i.e., $[H^+]_{y=0}/[H^+]_{inlet}$ vs distance from inlet) at various values of pH$_{inlet}$ and flow rate (Figure 3a and 3b). The homogeneous chemical reactions therefore have a negligible effect on the rate coefficients used to fit the experimental data.
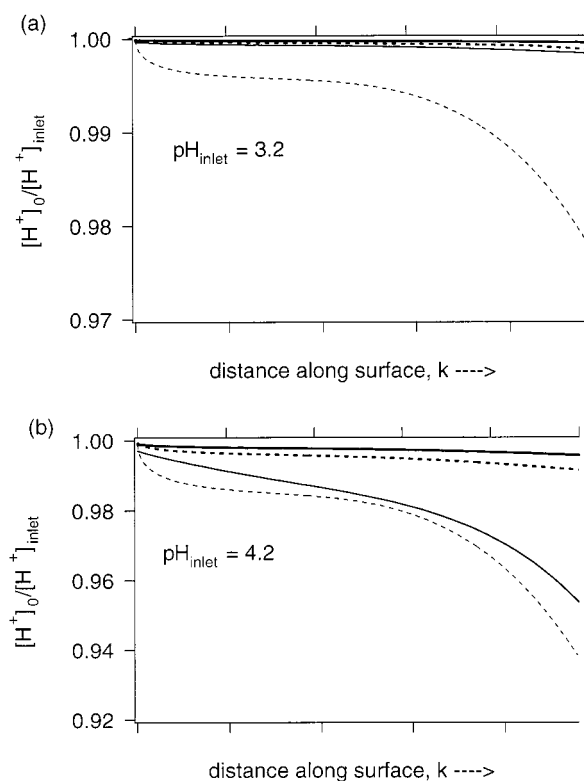
Surface Morphology of Magnesite (104)

*J. Phys. Chem. B, Vol. 106, No. 26, 2002* **6701**



**Figure 3.** Calculated normalized proton surface concentration ($[H^+]_{y=0}/[H^+]_{inlet}$) versus position along the sample surface at (a) pH = 3.2 and (b) pH = 4.2. Thin lines correspond to a flow rate of $7.52 \times 10^{-5}$ cm$^3$ s$^{-1}$ and thick lines to a flow rate of $7.52 \times 10^{-4}$ cm$^3$ s$^{-1}$. Dashed and solid lines are the result of inclusion and exclusion, respectively, of the homogeneous chemical kinetics. The total distance represented on the ordinate is approximately 0.94 mm with the AFM tip position located at 0.86 mm.

This observation indicates that our inclusion of the homogeneous terms was unnecessary and that in these experiments, the heterogeneous reaction is so sluggish that the approximation $[H^+]_{y=0} \approx [H^+]_{inlet}$ is valid to within a few percent relative error. At lower flow rates, the homogeneous chemical reactions would have a marked influence on the near surface proton concentration. In the more general case, where the products of homogeneous chemical reactions may interact with the solid surface, it is necessary to account for these reactions.

It is now possible to construct a plot of the observed limiting dissolution flux as a function of $-\log[H^+]_{y=0}$. These data are shown in Figure 4 with the dissolution flux presented on a log scale. From Figure 4 it is clear that there is a change in the slope of the data points at about $-\log[H^+]_{y=0} = 4.2$. Above $-\log[H^+]_{y=0} = 4.2$, the dissolution flux appears to be strongly dependent on $-\log[H^+]_{y=0}$ with a slope of approximately unity whereas below $-\log[H^+]_{y=0} = 4.2$, the slope is small.

Representative AFM images corresponding to the data points in Figure 4 are shown in Figure 5. A comparison of the images acquired at pH = 4.2 (Figure 5b) and pH = 5.0 (Figure 5a) reveals that there is little difference in the observed surface and step morphology under these two sets of conditions. However, the density of + steps increases by approximately an order of magnitude in going from pH = 5.0 to pH = 4.2 (note differences in lateral scale for Figure 5a and 5b). We also note the presence of numerous monolayer etch pits in the terraces under these conditions. An observable change in the step edge orientation of etch pits is noted when comparing the images taken at pH = 3.2 (Figure 5c) and 2.0 (Figure 5d) to those taken at higher pH. Specifically, the $[48\bar{1}]_+$ and $[\bar{4}41]_+$ steps become vicinal
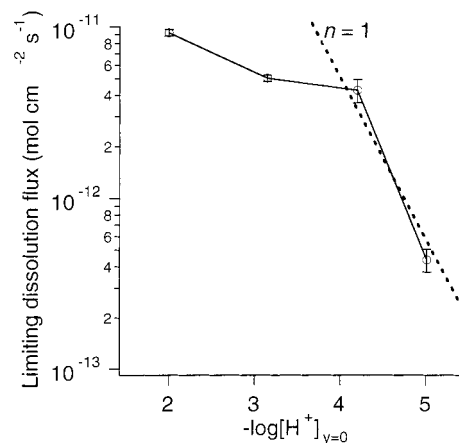


**Figure 4.** Plot of dissolution flux (log scale) versus $-\log[H^+]_{y=0}$. The dashed line with a slope of 1 (i.e., $n = 1$) demonstrates the inadequacy of a simple 1st order mechanism in describing the experimental data.
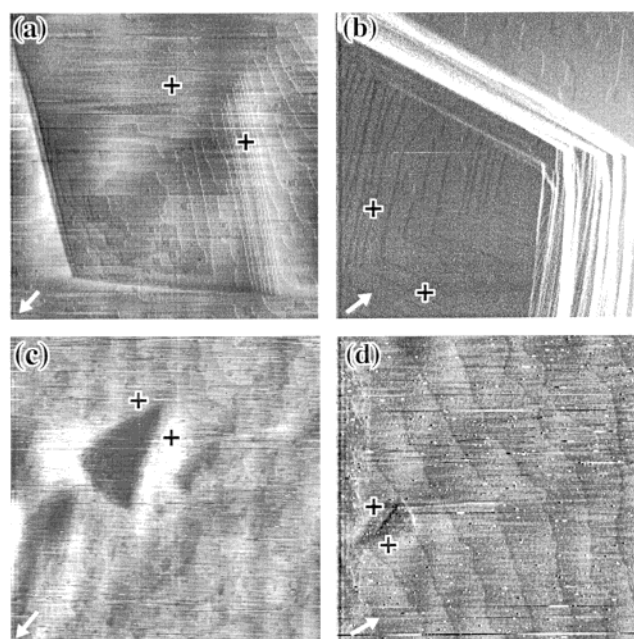


**Figure 5.** Representative AFM images taken from sequences used to calculate the dissolution fluxes in Figures 2 and 4. (a) pH = 5.0, image size: $6.7 \times 6.7 \mu$m; (b) pH = 4.2, image size: $2.0 \times 2.0 \mu$m; (c) pH = 3.2, image size: $7.0 \times 7.0 \mu$m; (d) pH = 2.0, image size: $6.6 \times 6.6 \mu$m. Arrows show the projection of the $c$-axis rising from the plane of the page. "+" symbols are placed amidst or in the vicinity of + steps in each image.

toward $[42\bar{1}]$ whereas the $[48\bar{1}]_-$ and $[\bar{4}41]_-$ steps become vicinal toward [010] in going from pH = 4.2 to pH = 3.15. The velocity of the + steps (determined perpendicular to the step direction), $v_+$, are shown as a function of $-\log[H^+]_{y=0}$ in Figure 6. Within the limits of experimental uncertainty, $v_+$ does not vary significantly with pH over the entire experimental pH range. It is not surprising that $v_+$ is independent of pH when the dissolution flux is weakly dependent on pH, but it is somewhat unexpected that there is no apparent change in $v_+$ that might correlate with the strong dependence of dissolution flux on $-\log[H^+]_{y=0}$ in the range 4.2 < pH < 5.0.

## 4. Discussion

The very weak influence of $[H^+]_{y=0}$ on dissolution flux below $-\log[H^+]_{y=0} = 4.2$ is consistent with a recent room-temperature dissolution study of magnesite suspensions by Pokrovsky and
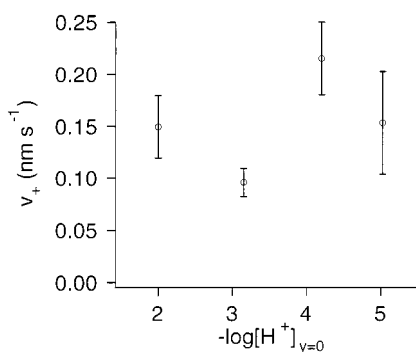
**Figure 6.** Velocity of $+$ steps, $v_+$ versus $-\log[H^+]_{y=0}$. Within the experimental uncertainty, the step velocity does not depend significantly on $-\log[H^+]_{y=0}$.

Schott.[35] Previous results from a variable temperature AFM study of magnesite dissolution[36] in which convective mass transport was not defined showed similar results although the observed dependence of flux on pH in that study was stronger over the same range of bulk pH conditions. An earlier study of magnesite dissolution by Chou et al.[6] showed approximately first-order kinetics in the same range of bulk pH. The discrepancy between the data of Pokrovsky and Schott and that of Chou et al. was explained in Pokrovsky and Schott as being attributed to Chou et al. not performing their experiments at constant ionic strength. However, the discrepancy between these two data sets occurs primarily at bulk pH values where Pokrovsky and Schott show little, if any, ionic strength effect in their data. It may therefore be suggested that ionic strength effects do not explain the discrepancy. Mass transport, on the other hand, may play a role in some of the previous experimental reports and thus provide a possible explanation for experimental discrepancies.

**Simple $n^{th}$ Order Kinetic Model.** The data presented in Figure 4 represent the limiting dissolution flux versus surface proton concentration. As discussed above for the case of a simple 1st order heterogeneous rate expression applied to the convective-diffusion problem, we may extend the conclusion to state that the data are not at all consistent with *any* simple $n^{th}$ order mechanism. The mechanistic scheme outlined by Compton and Unwin[10] for the dissolution of calcite included the likely sequence of elementary reaction steps that describe the overall dissolution reaction of calcite with protons in acidic solutions. In this scheme, depending on the slowest reaction step, Compton and Unwin concluded that one of three reaction orders (with respect to the surface proton concentration) were possible; $n = 1/2$, $n = 1$, or $n = 2$. Higher orders also would be permissible in this scheme by assuming a larger number of protons involved in the formation of a surface activated complex as proposed by Pokrovsky and Schott.[35] In the scheme described by Compton and Unwin, however, it was assumed that $[H^+]_{y=0}/K \ll 1$, where $K$ is a proton desorption equilibrium constant, so that only a small fraction of surface sites would be protonated. A more general approach (see below) would account for the case when $[H^+]_{y=0}/K$ is not small. It is possible to describe our data with a 1st order rate equation over a relatively narrow range of pH, but it should be emphasized that the Compton and Unwin model needs to be evaluated in the case of arbitrary $[H^+]_{y=0}/K$. Utilizing the concepts of this model enables us to conclude that the exchange of protons with surface sites must be relatively fast and that the overall rate of reaction might be best correlated to the concentration of surface *adsorbed* protons, as we will now examine.

**Langmuir or Surface Complexation Model.** Because adsorption of protons to a solid surface is ultimately limited by the total number of available adsorption sites, the kinetics of proton promoted dissolution will in general be a nonlinear function of surface proton concentration except at relatively low adsorption densities. Therefore, we may consider the magnesite surface to consist of a finite number of proton adsorption sites per unit area, $\sigma_{max}$, where the fraction of available sites possessing an adsorbed proton (i.e., surface coverage, $\theta$) obeys the Langmuir isotherm

$$\theta = \frac{K'_{ads}[H^+]_{y=0}}{1 + K'_{ads}[H^+]_{y=0}} = \frac{\sigma}{\sigma_{max}} \qquad (16)$$

where $K'_{ads}$ is the conditional equilibrium constant (e.g., Casey and Sposito[37]), containing the rational activity coefficients for the surface species and describing the relationship between adsorption density and proton concentration at the surface of the solid. In applying eq 16 to our problem, we make the approximation (i.e., by neglecting the electrostatic free energy contribution to $K'_{ads}$)

$$K'_{ads} \approx K_{int}^{-1}\gamma_{H^+} \qquad (17)$$

where $K_{int}$ is the intrinsic equilibrium constant for the following reaction[38]
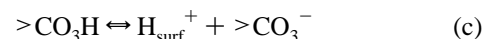
$$>CO_3H \leftrightarrow H_{surf}^+ + >CO_3^- \qquad (c)$$

$$K_{int} = \frac{(H^+)_{surf}(>CO_3^-)}{(>CO_3H)} \qquad (18)$$

In eq 18, parentheses imply activities and the symbol ">" implies a surface-attached species. To apply this model to the solution of the convective-diffusion equation, we need to determine the new surface rate equation to use as one of the boundary conditions. If desorption of the protonated surface sites is the rate-limiting step, then eq 10 must be written as

$$J = k_n[>CO_3H]^n \qquad (19)$$

where $k_n$ is the empirical $n^{th}$ order surface kinetic detachment coefficient. For $n > 1$ in eq 19, a more complicated transition state than simple monomeric desorption (i.e., $n = 1$) is inferred. Because we have no means for direct experimental measurement of $[>CO_3H]$ in these experiments and recognizing that $[>CO_3H] = \theta \cdot \sigma_{max}$, we can write eq 19 in terms of quantities more readily available

$$J = k_n(\theta\sigma_{max})^n = k'_n\left(\frac{K'_{ads}[H^+]_{y=0}}{1 + K'_{ads}[H^+]_{y=0}}\right)^n \qquad (20)$$

where $k'_n = k_n(\sigma_{max})^n$. We note that our use of a Langmuir model for the adsorption reaction implicitly ignores the influence of surface potential (or surface proton charge) on $K'_{ads}$. Without reasonable knowledge of $\sigma_{max}$, it is only possible to determine $k'_n$, the limiting dissolution flux at low pH, and therefore no information regarding the kinetic detachment coefficient, $k_n$, is obtained. A slightly different form from eq 20 is obtained if multiple protonation reactions, with similar equilibrium constants, give rise to the activated complex.

By assuming negligible temperature and pressure dependence to $K_{int}$ (= $2.24 \times 10^{-5}$ at 25 °C and 1 atm) up to 60 °C and 10

Surface Morphology of Magnesite (104)

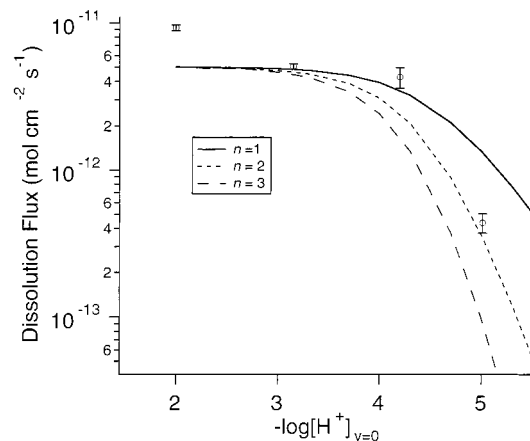*J. Phys. Chem. B, Vol. 106, No. 26, 2002* **6703**



**Figure 7.** Comparison of the experimental and calculated dissolution flux using a Langmuir adsorption model for the surface rate function. Solid, short-dashed, and long-dashed lines correspond to $n = 1$, $n = 2$, and $n = 3$ cases, where $n$ represents the number of adsorbed protons associated with the detachment complex.

bar $N_2$, we utilize the value obtained at 25 °C and $\sim$1 bar by Pokrovsky et al.[38] We may then combine eqs 10 and 20 for the Langmuir model to give

$$C_{0,k}^{H^+} = C_{1,k}^{H^+} \left[ \frac{D_{H^+}(1 + K'_{ads}C_{0,k}^{H^+})^n}{k'_n \Delta y (K'_{ads}C_{0,k}^{H^+((n-1)/n)})^n + D_{H^+}(1 + K'_{ads}C_{0,k}^{H^+})^n} \right] \quad (21)$$

This equation is solved by iteration where the initial value of $C_{0,k}^{H^+}$ must be stipulated. The only matrix coefficient modifications necessary to employ the new boundary condition eq 20 are

$$b_1^{H^+} = \frac{-(\lambda_y^{H^+} + \lambda_{v_y})}{\lambda_{v_d}}$$

$$\left[ \frac{D_{H^+}(1 + K'_{ads}C_{0,k}^{H^+})^n}{k'_n \Delta y (K'_{ads}C_{0,k}^{H^+((n-1)/n)})^n + D_{H^+}(1 + K'_{ads}C_{0,k}^{H^+})^n} \right] + \frac{2\lambda_y^{H^+} + \lambda_{v_y} + \lambda_{v_d}}{\lambda_{v_d}} \quad (22)$$

$$d_1^{HCO_3^-} = C_{1,k}^{HCO_3^-} - \frac{k_{H_2CO_3} C_{1,k}^{H^+} C_{1,k}^{HCO_3^-}}{K_{H_2CO_3} + C_{1,k}^{H^+} + C_{1,k}^{HCO_3^-}} + \frac{(\lambda_y^{HCO_3^-} + \lambda_{v_y})}{\lambda_{v_d}} \left[ \frac{\Delta y k'_n}{D_{HCO_3^-}} \left( \frac{K'_{ads}C_{0,k+1}^{H^+}}{1 + K'_{ads}C_{0,k+1}^{H^+}} \right)^n \right] \quad (23)$$

In the $n = 1$ case, the experimental data points from Figure 4 are not well represented (in Figure 7) by the theoretical prediction using the value of $K_{int}$ determined by Pokrovsky et al. at 25 °C. Standard enthalpies for proton adsorption (on oxide minerals) are almost always negative (e.g., Casey and Sposito[37] and references therein), implying that $K_{int}$ will increase with increasing $T$ (i.e., Van't Hoff equation). Therefore, our assumption that there is negligible temperature dependence to $K_{int}$ is probably faulty and the result, by including this temperature dependence, would be a shift of the theoretical $n = 1$ curve in Figure 7 toward lower pH. This however, does not improve the overall fit to the experimental data. Accounting for any

zeroth order reaction ($k_0$) would only worsen the fit, so it is apparent that the fit could only be improved by utilizing a larger value of $n$. Expected results for $n = 2$ and $n = 3$ are shown in Figure 7. In the $n = 2$ case, the experimental points are described by the theoretical predictions better than in the $n = 1$ case. The agreement between experiment and model are worse again in the $n = 3$ case although now our neglect of the zeroth order process may no longer be justified around pH = 5. Given the uncertainty in $K_{int}$ and $k_0$ at 60 °C and the relatively few points representing the experimental data, we do not believe a best-fit value for $n$ should be reported at this time. It is clear however that the preequilibration of the magnesite surface with respect to adsorption of near surface protons describes the general dissolution behavior at least in the range 3.2 < pH < 5.0. The observed doubling in dissolution flux from pH = 3.2 to pH = 2.0 is significant based on the uncertainty of the local flux measurements, but there is no reported experimental evidence elsewhere to suggest that this increase might be associated with protonation of additional surface sites.

**Phenomenology of the Surface.** From the experimental results above (Figure 6), we have established that the velocity of + steps that define the etch pit shape does not change significantly with $-\log[H^+]_{y=0}$. However, the local dissolution flux, $J(x, z)$, should be proportional to the product of the step velocity $v$, and the surface slope $p$

$$J(x, z) = p_\pm(x, z)v_\pm(x, z)\Omega^{-1} \quad (2\text{-}1)$$

This is an equivalent form of eq 2. In general, $p$ and $v$ are definite functions of position on the surface when mass transport in the bulk plays a role. The experimental data show that we may neglect any positional influences on dissolution flux due to mass transport. Therefore, assuming that microheterogeneities in the surface such as outcropping line defects and stacking faults do not influence the particular observations that we have made, we can write eq (2−1) above as

$$J = p_\pm v_\pm \Omega^{-1} \quad (2\text{-}2)$$

Surface heterogeneities can create a situation where the local flux may be higher in regions where defects exist, but our assumption is that our sampling of the surface structure and kinetics is representative. With step velocity varying little over the range of experimental conditions, the "pH-dependent" observable must be $p$.

**Surface Morphology Considerations Related to Langmuir Model.** The strongest influence of pH on dissolution flux was observed in the range 4.2 < pH < 5.0, where the surface step density changes were found to be the principal manifestation of changes in pH . If proton adsorption in this pH range occurs at the step edges, then we would expect that the step velocity would increase with decreasing pH. The observation that step velocity does not change with pH suggests that proton adsorption occurs at adions (i.e., ions adsorbed on top of the terraces) in this pH range. In terms of unsatisfied coordination to the crystalline lattice, we expect this type of situation where the degree of protonation of surface species at a given pH would follow the order: adions > kinks > steps > terraces. In this case, the increase in concentration of protonated adions would increase the undersaturation on the terraces leading to a decrease in the critical size of a two-dimensional nucleus, resulting in larger step density. This is the predicted result regardless of the type of dissolution "mechanism" (i.e., dissolution at dislocations or two-dimensional nucleation). We emphasize here that the change in step orientation within etch pits is not observed

until the pH drops below pH = 4.2, implying that significant proton adsorption at steps (or kinks) occurs below pH = 4.2. The simple Langmuir model discussed above is therefore only consistent with the AFM observations in this pH range (4.2–5.0) if $K_{int}$ at kinks and step edges, $K_{kinks}$ and $K_{steps}$, is significantly larger than $K_{int}$ for adions, $K_{adions}$. To describe the change in step orientation that occurs as the pH is decreased below pH = 4.2, a more detailed model that accounts for $K_{kinks}$ and $K_{steps}$ would need to be devised.

If there is not a canonical progression of adsorption constants, contrary to what we have inferred above, then the fairly simple Langmuir model is more a fortuitous success than a realistic model for describing the dissolution behavior. We base this argument on the Langmuir model assumption that there exists a fixed surface density of potential proton adsorption sites, $\sigma_{max}$. When $pH_{y=0} \gg pK_{int}$, these sites are present, here as the majority of $\sigma_{max}$, in the unprotonated form. The increase in step density with increase in $[H^+]_{y=0}$ therefore implies a change (i.e., increase) in $\sigma_{max}$ if the steps were involved in the adsorption of protons in the range $4.2 < pH < 5.0$, which is contrary to the Langmuir model assumption. A possible pitfall to this line of reasoning is that we do not know the surface concentration of adions, which we have implicitly assumed to be small, relative to the surface concentration of step sites. If these concentrations turn out to be comparable, then any change in step density does not significantly change the number of available sites for adsorption. In this case, the entire surface behaves as a uniform source (not an *ideal* source, however, as in the case of a bulk diffusion-controlled source) of dissolved components regardless of the distance to the nearest step. The limiting dissolution flux then would be determined by desorption from any part of the surface, suggesting only a minor role of surface morphology in determining dissolution flux.

The particular "mechanism" that governs the rate of magnesite dissolution is not determinable from the discussions above. From the images in Figure 5, one may conclude that etch pits of the multilayer variety are ubiquitous to the surface morphology. The types of defects that give rise to these etch pits may vary in dimension (i.e., finite inclusions, dislocation loops, linear, or planar defects) and in character (i.e., screw, edge, combination, or multiple dislocation). Therefore, the manner in which these defects are etched (i.e., spiral dissolution, two-dimensional nucleation) will ultimately determine the most appropriate model for the dissolution process. Only by assuming that one specific type of defect dominates the dissolution flux over the entire mineral surface may there be a simple integer rate order that appropriately describes the dissolution kinetics.[39] This assumption (at least microscopically) was implicit in our treatment of the AFM flux data. Due to the difficulty in observing the etch pit formation process (as opposed to the relative ease at which the sources of growth hillocks may be observed by AFM during precipitation), the only signals we may observe are the step density, step velocity, and step morphology. Therefore, any model we attempt to test should be based upon this type of phenomenology. To develop a more complicated model that accounts for the defects would not be justified, as we have no information on the nature of the defects influencing our observations.

## 5. Summary

The most appropriate model that we considered for describing the dissolution flux of magnesite in acidic solution is that of a Langmuir (or Surface Complexation) model for proton adsorption. The *apparent* surface kinetic detachment coefficient, $k'_n$

was determined from the limiting dissolution flux at $[H^+]_{y=0} \gg K_{int}$ ($k'_n = 5 \times 10^{-12}$ mol cm$^{-2}$ s$^{-1}$). The $n^{th}$ order surface kinetic detachment coefficient, $k_n$, could not be determined because there are no quantitative experimental data to estimate a value for $\sigma_{max}$, and the value for $K_{int}$ at 60 °C was taken from data obtained at 25 °C. The surface and step morphology based on AFM images at different values of pH suggested that a single $K_{int}$ is not sufficient to describe the protonation reaction on the magnesite surface. Instead, the degree of protonation of any particular site (i.e., Adion, kink, step, terrace) at fixed pH will depend on the $K_{int}$ for that particular site.

**Appendix A.** By assuming reaction a to be at equilibrium, we may write

$$K_{H_2CO_3}[H_2CO_3] = [H^+][HCO_3^-] \qquad (A1)$$

As in Compton and Unwin,[10] the rate of change of concentration of the homogeneous species $H^+$, $HCO_3^-$, and $H_2CO_3$ can be written

$$\frac{d[H^+]}{dt} = k_{-a}[H_2CO_3] - k_a[H^+][HCO_3^-] \qquad (A2)$$

$$\frac{d[HCO_3^-]}{dt} = k_{-a}[H_2CO_3] - k_a[H^+][HCO_3^-] \qquad (A3)$$

$$\frac{d[H_2CO_3]}{dt} = k_a[H^+][HCO_3^-] - (k_{H_2CO_3} + k_{-a})[H_2CO_3] \qquad (A4)$$

where $k_{H2CO3}$ is the forward rate constant for reaction b, and $k_a$ and $k_{-a}$ are the respective forward and reverse rate constants for reaction a. Differentiating both sides of (A1) with respect to time, reorganizing and recognizing that the rhs of both (A2) and (A3) are equal leads to

$$\frac{d[H_2CO_3]}{dt} = \frac{([HCO_3^-] + [H^+])}{K_{H_2CO_3}} \frac{d[HCO_3^-]}{dt}$$

Substituting the rhs of this result into the lhs of (A4) and the rhs of (A3) into the rhs of (A4), and solving for $d[HCO_3^-]/dt$ results in

$$\frac{d[HCO_3^-]}{dt} = \frac{-k_{H_2CO_3}[H^+][HCO_3^-]}{[HCO_3^-] + [H^+] + K_{H_2CO_3}} = \frac{d[H^+]}{dt} \qquad (A5)$$

## References and Notes

(1) Fredrickson, J. K.; Brockman, F. J.; Bjornstad, B. N.; Long, P. E.; Li, S. W.; McKinley, J. P.; Wright, J. V.; Conca, J. L.; Kieft, T. L.; Balkwill, D. L. *Geomicrobiol. J.* **1993**, *11*, 95.

(2) Berner, R. A.; Lasaga, A. C.; Garrels, R. M. *Am. J. Sci.* **1983**, *283*, 641.

(3) Garrels, R. M.; MacKenzie, F. T. *Evolution of Sedimentary Rocks*; W. W. Norton and Company, Inc.: New York, 1971.

(4) Department of Energy, Offices of Science and Fossil Energy. "Carbon Sequestration: State of the Science – A Working Paper for Road Mapping Future Carbon Sequestration R&D", 1999.

(5) Gunter, W. D.; Wiwchar, B.; Perkins, E. H. *Mineral. and Petrol.* **1997**, *59*, 121.

(6) Chou, L.; Garrels, R. M.; Wollast, R. *Chem. Geol.* **1989**, *78*, 269.

(7) Schott, J.; Brantley, S.; Crerar, D.; Guy, C.; Borcsik, M.; Willaime, C. *Geochim. Cosmochim. Acta* **1989**, *53*, 373.

(8) Shiraki, R.; Rock, P. A.; Casey, W. H. *Aquatic Geochem.* **2000**, *6*, 87.

(9) Plummer, L. N.; Wigley, T. M. L.; Parkhurst, D. L. *Am. J. Sci.* **1978**, *278*, 179.

(10) Compton, R. G.; Unwin, P. R. *Philos. Trans. Royal Soc. London A* **1990**, *330*, 1.

(11) Coles, B. A.; Compton, R. G.; Suárez, M.; Booth, J.; Hong, Q.; Sanders, G. H. W. *Langmuir* **1998**, *14*, 218.

(12) Sjöberg, E. L.; Rickard, D. T. *Chem. Geol.* **1984**, *42*, 119.

(13) Sjöberg, E. L.; Rickard, D. T. *Geochim. Cosmochim. Acta* **1984**, *48*, 485.

(14) Unwin, P. R.; Barwise, A. J.; Compton, R. G. *J. Colloid Interface Sci.* **1989**, *128*, 208.

(15) Vekilov, P. G.; Monaco, L. A.; Rosenberger, F. *J. Cryst. Growth* **1995**, *148*, 289.

(16) Lüttge, A.; Bolton, E. W.; Lasaga, A. C. *Am. J. Sci.* **1999**, *299*, 652.

(17) Coles, B. A.; Compton, R. G.; Booth, J.; Hong, Q.; Sanders, G. H. W. *J. Chem. Soc., Chem. Commun.* **1997**, 619.

(18) Higgins, S. R.; Jordan, G.; Eggleston, C. M.; Knauss, K. G. *Langmuir* **1998**, *14*, 4967.

(19) Higgins, S. R.; Bosbach, D.; Eggleston, C. M.; Knauss, K. G. *J. Phys. Chem. B* **2000**, *104*, 6978.

(20) Jordan, G.; Higgins, S. R.; Eggleston, C. M.; Knauss, K. G.; Schmahl, W. W. *Geochim. Cosmochim. Acta* **2001**, *65*, 4257.

(21) Higgins, S. R.; Eggleston, C. M.; Knauss, K. G.; Boro, C. O. *Rev. Sci. Instrum.* **1998**, *69*, 2994.

(22) Compton, R. G. ftp://joule.pcl.ox.ac.uk/pub/rgc/afmvmaps/.

(23) Hong, Q.; Suárez, M. F.; Coles, B. A.; Compton, R. G. *J. Phys. Chem. B* **1997**, *101*, 5557.

(24) Jordan, G.; Higgins, S. R.; Eggleston, C. M. *Am. Mineral.* **1999**, *84*, 144.

(25) Wilkins, S. J.; Suarez, M. F.; Hong, Q.; Coles, B. A.; Compton, R. G.; Tranter, G. E.; Firmin, D. *J. Phys. Chem. B* **2000**, *104*, 1539.

(26) Morton, K. W. *Numerical Solution of Convection-Diffusion Problems*; Chapman and Hall: London, 1996; Vol. 12.

(27) Fosdick, L. E.; Anderson, J. L. *Anal. Chem.* **1988**, *60*, 156.

(28) Compton, R. G.; Pilkington, M. B. G.; Stearn, G. M. *J. Chem. Soc., Faraday Trans. 1* **1988**, *84*, 2155.

(29) Suárez, M. F.; Compton, R. G. *J. Phys. Chem. B* **1998**, *102*, 7156.

(30) Lapidus, L.; Pinder, G. F. *Numerical Solution of Partial Differential Equations*; Wiley: New York, 1982.

(31) Compton, R. G.; Pritchard, K. L. *Philos. Trans. R. Soc. London A* **1990**, *330*, 47.

(32) Harned, H. S.; Owen, B. B. *Physical Chemistry of Electrolytic Solutions*, 2nd ed.; Reinhold Book Corporation: New York, 1950.

(33) Wissbrun, K. F.; French, D. M.; Patterson, A. *J. Phys. Chem.* **1954**, *58*, 693.

(34) Patel, R. C.; Boe, R. J.; Atkinson, G. *J. Solution Chem.* **1973**, *2*, 357.

(35) Pokrovsky, O. S.; Schott, J. *Geochim. Cosmochim. Acta* **1999**, *63*, 881.

(36) Higgins, S. R.; Jordan, G.; Eggleston, C. M. *Geochim. Cosmochim. Acta* **2002**, in press.

(37) Casey, W. H.; Sposito, G. *Geochim Cosmochim Acta* **1992**, *56*, 3825.

(38) Pokrovsky, O. S.; Schott, J.; Thomas, F. *Geochim. Cosmochim. Acta* **1999**, *63*, 863.

(39) Teng, H. H.; Dove, P. M.; DeYoreo, J. J. *Geochim. Cosmochim. Acta* **2000**, *64*, 2255.